Title
Flow and Arrest in Stressed Granular Materials

Authors
Srivastava, Ishan
Silbert, Leonardo E
Lechman, Jeremy B
et al.

Publication Date
2021-04-01

Peer reviewed

Flow and Arrest in Stressed Granular Materials

Ishan Srivastava*
Center for Computational Sciences and Engineering, Lawrence Berkeley National Laboratory, Berkeley, CA 94720, USA

Leonardo E. Silbert
School of Math, Science, and Engineering, Central New Mexico Community College, Albuquerque, NM 87106, USA

Jeremy B. Lechman and Gary S. Grest
Sandia National Laboratories, Albuquerque, NM 87185, USA

Flowing granular materials often abruptly arrest if not driven by sufficient applied stresses. Such abrupt cessation of motion can be economically expensive in industrial materials handling and processing, and is significantly consequential in intermittent geophysical phenomena such as landslides and earthquakes. Using discrete element simulations, we calculate a flow-arrest state diagram for granular materials under the conditions of constant applied pressure and shear stress, which are also most relevant in practice. Here the material can dilate or compact, and flow or arrest, in response to the applied stress. Our simulations highlight that under external stress, the intrinsic response of granular materials is characterized by uniquely-defined nonequilibrium steady states of flow or arrest, which are highly sensitive to interparticle friction. While the flowing states can be equivalently characterized by volume fraction, coordination number or internal stress ratio, to characterize the states of shear arrest, one needs to also consider the structural anisotropy in the contact network. We highlight the role of dilation in the flow-arrest transition, and discuss our findings in the context of shear jamming and discontinuous shear thickening.

INTRODUCTION

A remarkable property of granular materials is their ability to exist in both solid-like and fluid-like states [1]. The fluid-like properties of these materials are commonly utilized during their production, handling and transportation in several industries such as pharmaceutical, agriculture and construction, while flowing granular materials are also observed in important geophysical phenomena such as flow of fault gouge in earthquakes [2] and debris flow in landslides [3]. Frequently, however, the flowing granular material abruptly arrests leading to significant economic and geophysical consequences, such as clogged flows [4] and cessation of sediment transport in riverbeds [5]. Such flow-arrest transitions are not limited to dry granular materials, but are also observed in dense shered suspensions [6, 7], where the suspension viscosity dramatically increases by several orders of magnitude upon external stressing. Although the distinctions between solid-like and fluid-like states of granular materials have been thoroughly studied [8], a unified understanding of the nonequilibrium flow-arrest transition is still lacking. Particularly, the role of external boundary conditions on flow-arrest transitions, while crucial, has been not been well-characterized.

A well-known jamming phase diagram for frictionless particles predicts that a potentially flowing state can be arrested by increasing its solid volume fraction ϕ or increasing its internal shear stress τ across an yield stress line [9]. The scenario is more complicated for frictional particles with the emergence of solid-like fragile and shear-jammed states at low volume fractions [10]. In practice however, the volume fraction of granular materials is rarely controlled and the material responds to external stresses by compacting under pressure and compacting or dilating under shear [11]. The dynamics of granular materials under controlled pressure p are better understood through $\mu(I)$ and $\phi(I)$ constitutive relationships, where $\mu = \tau/p$ is a dimensionless stress ratio, and $I = \dot{\gamma} d\sqrt{\rho/p}$ is a dimensionless inertial number [1]. Here $\dot{\gamma}$ is strain rate of flow, d is mean particle size and ρ is particle density. Previous experiments [12, 13] and simulations [14, 15] have demonstrated that granular materials flow only when μ exceeds a critical value along with the material attaining a critical ϕ. These critical conditions depend significantly on interparticle friction, as shown in previously in simulations [16] and also predicted by the critical state theory of soil mechanics [17]. However, these constitutive relationships do not predict the state of flowing granular material that will eventually arrests when μ is reduced below the critical value. Furthermore, these relationships are isotropic and do account for dominant microstructural features such as directional force chains that are observed in experiments at the flow-arrest transition [10].

Boundary conditions play a crucial role in the rheological behavior of granular materials. Under a constant external pressure and applied strain rate, μ increases mono-

* isriva@lbl.gov

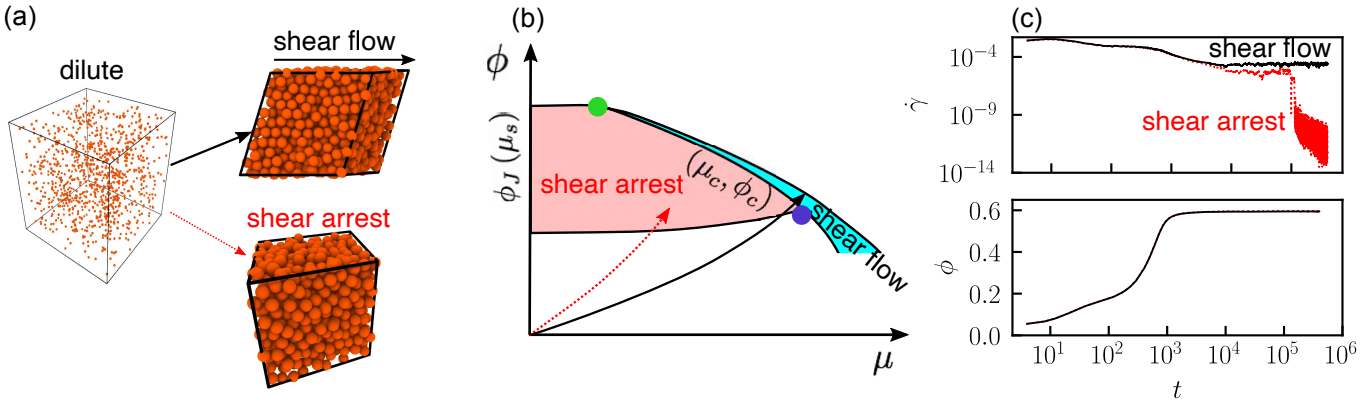

FIG. 1. (a) Schematic of the simulation method. The left image depicts a starting state at a dilute volume fraction. The black lines enclosing the particles denote triclinic periodic boundaries. The images on the right depict two possible nonequilibrium states upon the application of external pressure and shear stress: shear arrest and steady shear flow. (b) A schematic of the flow-arrest state diagram on the $\phi - \mu$ axes. The red and blue regions represent states of shear arrest and steady shear flow respectively. The boundary between the two regions is the critical state characterized by the pair (μ_c, ϕ_c). The green and blue dots represent the critical state for frictionless and high friction particles respectively. The white region outside red and blue regions is inaccessible in steady state. The y-axis at $\mu = 0$ represents the μ_s-dependent isotropic jamming volume fraction ϕ_J. (c) Evolution of strain rate $\dot{\gamma}$ (top) and volume fraction ϕ (bottom) with simulation time t for a case each of shear arrest (dotted red) and steady shear flow (solid black). In the bottom panel of (c), the two curves are almost coincident.

tonically with I and saturates at a critical value μ_c as $I \to 0$ in the quasi-static regime, whereas the ϕ decreases monotonically with increasing I reaching a critical value ϕ_c as $I \to 0$ [16]. The rheological response is significantly different when the material is not allowed to dilate or compact in response to shear flow at a constant volume fraction. In this case below a critical ϕ, the material can flow at all strain rates and it exhibits a continuous transition from inertial flow to plastic flow as the strain rate is increased, whereas a solid-like yield behavior is observed above this critical ϕ [18, 19]. However, the transition from fluid-like to solid-like states is discontinuous, which leads to chaotic dynamics [20] and a re-entrant jamming transition near a critical ϕ [21]. The situation becomes increasingly complex in some non-Brownian suspensions where external stresses can drive a frictional transition within the particle contact network [22] leading to a discontinuous increase in the suspension viscosity and shear jamming [6, 7]. The nature of boundary conditions dominantly governs the mechanics of such suspensions, as demonstrated by intriguing flow phenomena such as negative dynamic compressibility [23] and vorticity banding [24].

As such, a careful characterization of the flow-arrest transition as an intrinsic *bulk* property of granular materials requires three key considerations of the boundary conditions: (i) a constant external pressure as the natural boundary condition, where the material can dilate or compact as it flows or arrests. In addition to being the dominant boundary condition in practical applications of granular flows, constant pressure conditions are particularly well-suited for exploring granular flow dynamics near the critical jamming volume fraction where the magnitude of stress fluctuations can be quite large [25, 26]; (ii) a constant external stress rather than strain rate as the imposed driving force, which allows for a seamless transition between flowing and arrested states of granular materials [26, 27]; (iii) the avoidance of external walls or boundaries that can complicate the rheological response by flow localization [24, 28] and non-local effects [29].

In this work, we use stress-controlled discrete element simulations to analyze nonequilibrium states of steady shear flow and shear arrest along with their dependence on interparticle friction, by approaching the critical flow-arrest transition along the paths of constant pressure and shear stress. We propose state diagrams along $\phi - \mu$ and $Z - \mu$ axes that clearly distinguish between shear-arrested and steady flowing states of granular materials, where Z is the coordination number. We demonstrate that although the internal state of steady granular flow is uniquely represented by either μ, ϕ or Z, such uniqueness is very weak for shear-arrested states, which are better distinguished by a higher-order structural description of the particle contact network. We identify the contact fabric tensor as an important higher-order structural descriptor that uniquely represent the nonequilibrium states of both shear arrest and steady shear flow in granular materials. This finding has important consequences for constitutive modeling of granular materials across their fluid-like and solid-like states of existence. Lastly we discuss our findings in the context of shear jamming and highlight potential extensions of our simulations towards understanding the role of boundary conditions in discontinuous shear thickening of suspensions.

RESULTS

We simulate flow-arrest transition in granular materials by subjecting a dilute system of particles to constant external pressure p_a and shear stress τ_a (see *Materials and Methods*). The particles are initially contained in a cubic simulation cell that is periodic along all directions, as shown schematically in Fig. 1a. The simulation method allows for the dynamical evolution of all the three shear degrees of freedom along with the evolution of the volume of the simulation cell in response to applied stress and pressure. This deformation of the simulation cell is tracked by the time evolution of its triclinic periodic boundaries. Each simulation consists of $N = 10^4$ spherical particles whose diameters are uniformly distributed between $0.9d$ and $1.1d$. The particles interact through a linear spring-dashpot viscoelastic contact mechanical model, along with tangential Coulomb friction that is characterized by a coefficient of friction μ_s [16]. The tangential spring stiffness is set equal to the normal spring stiffness k_n, which is set to unity. The normal velocity damping constant is set as $\nu_n = 0.5$, and the tangential velocity damping constant is set as $\nu_t = 0.25$. In the present simulations, time is normalized by the characteristic timescale $t_c = \pi \left(2k_n/\rho d^3 - \nu_n^2/4\right)^{-1/2}$, which is the characteristic collision time between two particles [16]. The simulation time step is set to $0.02t_c$, and each simulation is run for at least $10^6 t_c$ total time. The spring constant sets the scale for stress in the system; therefore, all stresses are scaled by k_n/d.

The granular system initially responds to the applied stress by rapid compaction under the action of pressure along with significant shear straining, as shown by the evolution of deviatoric strain rate $\dot{\gamma}$ and volume fraction ϕ in Fig. 1c. After initial transients the system enters into a quasi-steady flow that is characterized by fluctuations around a mean value of $\dot{\gamma}$ and ϕ. At long times, the dynamical evolution of granular system exhibits two distinct phenomena as shown in Fig. 1a: (i) for low values of τ_a/p_a, the system enters into a dynamically arrested solid-like state resulting in a drop of $\dot{\gamma}$ by several orders of magnitude; (ii) for large enough values of τ_a/p_a the system continues to flow steadily around mean values of $\dot{\gamma}$ and ϕ.

Previously it was demonstrated that the dynamical arrest of dense granular flows is highly stochastic and the time for the flow to arrest exhibits a heavy-tailed distribution whose statistics diverge at a critical value of stress ratio μ [26]. However, the internal state of the granular material upon arrest is deterministic and depends on both μ and μ_s [30]. Based on these observations, we postulate a flow-arrest state diagram where nonequilibrium states of granular arrest exist at low μ and high ϕ, and states of steady granular flows exist at high μ and low ϕ, as also shown in a schematic in Fig. 1b. Under the action of external pressure and shear stress, it is expected that any state at high μ and high ϕ, or low μ and low ϕ are forbidden. At high μ greater than a friction-dependent critical μ_c, the system can not exist at arbitrarily high ϕ and will necessarily dilate to a volume fraction lower than a friction-dependent critical ϕ_c to achieve steady flow. Similarly, at low μ smaller than a critical μ_c, the shear stress is not large enough to drive steady granular flow and the material will compact into a shear-arrested solid under the action of external pressure. For the particular case of $\mu = 0$ that corresponds to isotropic jamming under external pressure and zero shear stress, the friction dependent jamming volume fraction $\phi_J(\mu_s)$ [31] is expected to be recovered, as indicated by the y-axis of the proposed state diagram in Fig. 1b. In the present simulations, the initial conditions correspond to $\mu = 0$ and a very low ϕ. After the external pressure and shear stress are switched on, the system will follow nonequilibrium paths to either granular flow or arrest depending upon the magnitude of τ_a/p_a, as shown in Fig. 1b. Although the state diagrams calculated in this paper are extracted from simulations starting from states with low μ and low ϕ, we have verified that they are robust to initial conditions by performing simulations with initial states at higher volume fractions.

States of Flow and Arrest

Simulations were performed for a range of frictions from $\mu_s = 0.0$ for frictionless particles to $\mu_s = 0.3$ that characterizes the high friction limit. Several applied stresses ranging from $\tau_a/p_a = 0.0$ for isotropic jamming to $\tau_a/p_a = 1.0$ were analyzed, and three simulations were run for each case of μ_s and τ_a/p_a. Although the results presented in the main text are for $p_a = 10^{-5}$, which corresponds to the hard-particle limit, no significant pressure dependence was observed for pressures $p_a = 10^{-4}$ and $p_a = 10^{-6}$ in accordance with similar previous observations [32] (see *SI Appendix* for state diagrams for these two pressures).

Figure 2a shows nonequilibrium states of shear arrest (open symbols) and steady shear flow (closed symbols) on a $\phi - \mu$ state diagram for various μ_s. The steady state behavior for a given case of μ_s and τ_a/p_a is treated as shear arrest (flow) if all three simulations for that case resulted in shear arrest (flow). In the vicinity of critical transition between arrest and flow, often not all three simulations resulted in shear arrest or flow within the simulation run time; these cases have been marked with an asterisk. This results from the stochastic nature of shear arrest and depends significantly on simulation run time and system size [26].

For steady flowing states, ϕ decreases rapidly and monotonically with increase in μ for all μ_s, thus indicating the dilating nature of granular flows. Furthermore, the one-to-one relationship between ϕ and μ implies that μ uniquely sets ϕ in steady granular flows for all μ_s, which has important consequences in constitutive modeling of granular materials [33]. This is similar to the predictions of the kinetic theory [34] and hydrodynamic models [35]

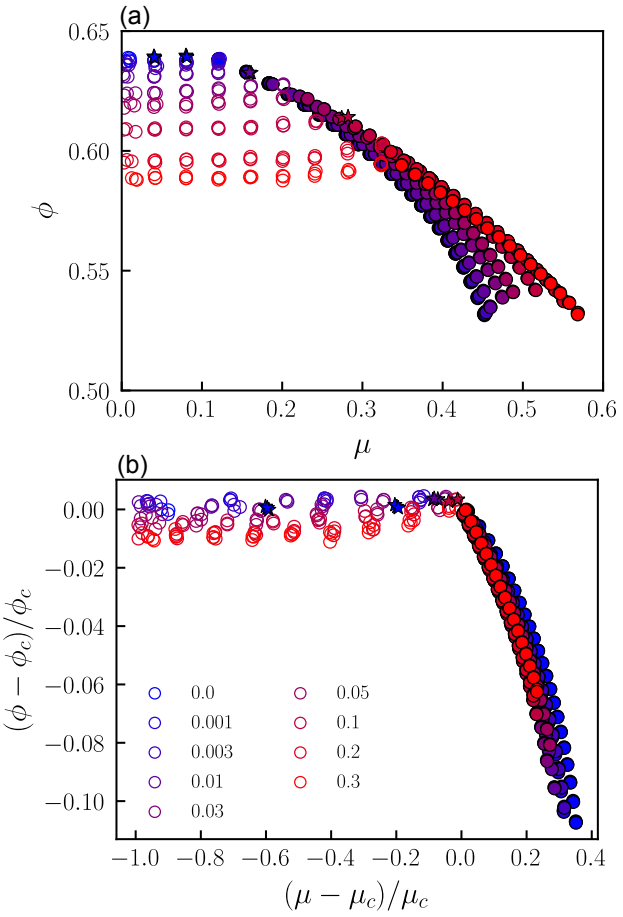

FIG. 2. (a) Nonequilibrium states of shear arrest (open symbols) and steady shear flow (closed symbols) on $\phi - \mu$ axes for different frictions μ_s (see the color legend in (b)). The asterisk denote states in the vicinity of the flow-arrest transition for which some simulations arrested and some flowed steadily at long times. (b) The state diagram in (a) shifted and normalized by the friction-dependent critical values μ_c and ϕ_c.

where such a relationship was determined between internal granular temperature and ϕ for granular flows. Unlike states of steady flow, a strong one-to-one relationship between μ and ϕ does not exist for the states of shear arrest, which all seem to possess nearly the same μ_s-dependent ϕ irrespective of μ. A slight increase in ϕ with μ is observed near the flow-arrest transition for particles with high friction, and this can possibly be attributed to rheological hysteresis in frictional particles [36]. Therefore, another internal variable beyond ϕ is required for a unique characterization of the internal state of shear arrest.

Considering closely the region of arrested states from our simulations, the isotropic jamming volume fraction (at $\mu = 0$) for frictionless particles $\phi_J = 0.64$ is equivalent to the random closed packing fraction, whereas $\phi_J = 0.59$ is observed for high friction, similar to previous simulations [31] and experiments [12, 13] on frictional particles. The critical flow-arrest transition for frictionless particles occurs at $\phi_c = 0.64$ and $\mu_c = 0.1 \pm 0.02$ (denoted by the green dot in the schematic in Fig. 1b), which is consistent with previous simulations [15] and experiments [13] on the rheology of frictionless particles. The equality $\phi_J = \phi_c = 0.64$ with the random closed packing fraction for frictionless particles confirms previous observations that frictionless particles do not need to dilate in order to begin flowing [15]. For particles with high friction, the critical flow-arrest transition occurs at $\phi_c = 0.59$ and $\mu_c = 0.34 \pm 0.01$ (denoted by the blue dot in the schematic in Fig. 1b), which is consistent with previous experiments [12, 13], simulations [16, 37] and predictions from the theory of critical state soil mechanics [17] for the onset of granular flow. Although μ_c and ϕ_c were estimated from the discrete data by demarcating the steady shear flow and shear arrested nonequilibrium states, these estimates match well with their more precisely calculated values in ref. [26] from the power-law divergence of the time for a flowing granular material before arrest. Using the estimated values of μ_c and ϕ_c, the shear arrest part of the state diagram is collapsed on to a nearly horizontal master curve for all μ_s by plotting $(\phi - \phi_c)/\phi_c$ vs. $(\mu - \mu_c)/\mu_c$, as shown in Fig. 2b. The very weak dependence of $\phi - \phi_c$ on $\mu - \mu_c$ for shear-arrested states also demonstrates that $\phi_J \approx \phi_c$, i.e., granular materials begin to dilate and flow at volume fractions that are nearly equal to their friction dependent isotropic jamming volume fractions.

Unlike shear arrest, the steady flowing part of the state diagram is not collapsed onto a similar master curve because $\mu - \mu_c$ and $\phi - \phi_c$ scale differently with the inertial number of flow, as shown in Fig. 3. Prior studies [16, 32] have provided estimates on friction dependent power-law scaling of $\mu - \mu_c \sim I^\alpha$ and $\phi_c - \phi \sim I^\beta$, and the results from our present simulations correspond well with the previously determined power-law scaling exponents.

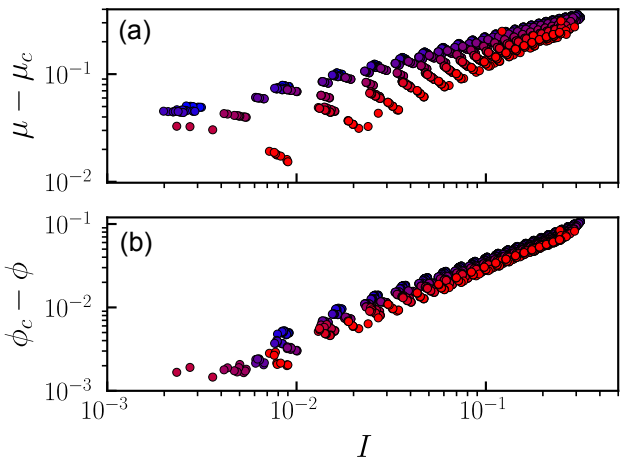

FIG. 3. Variation of (a) $\mu - \mu_c$ and (b) $\phi_c - \phi$ with the inertial number I for nonequilibrium states of steady shear flow. The different colors represent various frictions (see the color legend in Fig. 2b).

The Role of Coordination and Contact Fabric

The coordination of the grains in a granular system plays a key role in their properties both during jamming [38] and flow [39]. Previously, a constitutive model was proposed that incorporated the coordination number as an internal state variable in steady and unsteady quasi-static granular flows [40]. In this work, we define a coordination number $Z = 2N_c/N$, where N_c is the total number of contacts with non-zero normal forces. In Fig. 4a, Z for flow and arrested states is plotted as a function of μ for various μ_s. For frictionless particles, the coordination number at isotropic jamming $Z_J \approx 6$, whereas $Z_J \approx 4$ for particles with high friction, which is consistent with previous simulations [31, 41]. In a manner similar to ϕ, all the arrested states possess the same μ_s-dependent Z irrespective of μ. From the state diagram, critical values of friction-dependent Z_c were extracted, and all the shear-arrested states are collapsed on to a nearly horizontal master curve for all μ_s by plotting $(Z - Z_c)/Z_c$ vs. $(\mu - \mu_c)/\mu_c$, as shown in the inset of Fig. 4a. For flowing states, Z decreases rapidly and monotonically with μ for all μ_s, predominantly from the loss of contacts in the extension direction of simple shear flow [42]. For all steady flowing states, a unique one-to-one relationship exists between Z and μ as shown in Fig. 4a, in a manner similar to the relationship between ϕ and μ in Fig. 2a. Therefore for a given friction, the steady shear flowing state of a granular material can be uniquely identified by either μ, ϕ or Z as there exists a one-to-one relationship between these quantities.

Such a one-to-one relationship is very weak for shear-arrested states that possess nearly the same μ_s-dependent ϕ and Z regardless of μ, thus necessitating a more microstructure-sensitive metric for their characterization. It is expected that the topological structure of the particle contact network in an arrested granular system would be increasingly anisotropic with an increase with μ, resulting from directionally-dominant contact networks that are required to support the external shear stress [10, 30]. Therefore, a higher-order structural descriptor beyond isotropic measures such as ϕ and Z is required to distinguish such structural anisotropy in shear-arrested states. We quantify the structural of the contact network using a contact fabric tensor $\boldsymbol{A}_c$ [30, 43] whose second invariant a_c is a measure of the anisotropy in the contact network (see *Materials and Methods*). Figure 4b shows the dimensionless ratio a_c/Z for flowing and arrested states as a function of μ for various μ_s. Unlike ϕ and Z, there exists a one-to-one relationship between a_c and μ for the states of shear arrest. Furthermore, a linear relationship $a_c \sim \mu$ emerges as Z is nearly constant for all shear arrested states regardless of μ from Fig. 4a. Interestingly, the linear relationship between a_c/Z and μ is independent of μ_s (see the collapse of a_c/Z for all frictions in Fig. 4b), thus indicating that the internal state of a shear-arrested granular system containing weakly polydisperse spheres is uniquely characterized by its contact

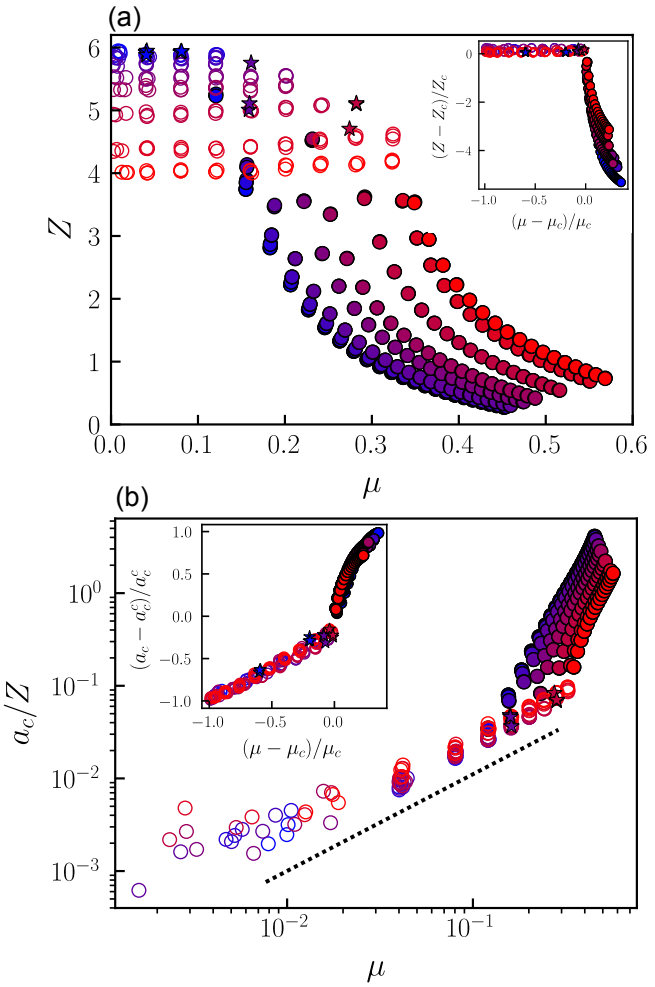

FIG. 4. Nonequilibrium states of shear arrest (open symbols) and steady shear flow (closed symbols) on $Z - \mu$ axes for different frictions μ_s (see the color legend in Fig. 2b). The asterisk denote states in the vicinity of the flow-arrest transition for which some simulations arrested and some flowed steadily at long times. The inset shows the state diagram shifted and normalized by the friction-dependent critical values Z_c and μ_c. (b) Contact fabric anisotropy a_c normalized by Z for the states of steady flow and arrest as a function of μ for different μ_s. The dotted line denotes a slope of unity. The inset shows the state diagram shifted and normalized by the friction-dependent critical values a_c^c and μ_c.

anisotropy irrespective of the friction. A critical friction-dependent fabric anisotropy a_c^c at the flow-arrest transition is extracted from the state diagram. The unique linear relationship between fabric anisotropy and stress ratio for all shear-arrested states regardless of friction is also seen by the collapse of $(a_c - a_c^c)/a_c^c$ vs. $(\mu - \mu_c)/\mu_c$ on to a linear master curve in the inset of Fig. 4b.

For steady flowing states above the critical flow-arrest transition, the ratio a_c/Z increases rapidly with μ as shown in Fig. 4b, with an observed scaling of $a_c/Z \sim \mu^{\xi}$, where ξ varies slightly with friction ranging from 3.8 for frictionless particles to 4.0 for particles with high fric-

tion. Unlike shear arrested states where there is no loss of coordination upon increasing μ, the super-linear increase in a_c with μ in flowing states is a consequence of directional alignment of the contacts along the compression direction in addition to a loss of coordination in the extension direction of shear flow [42]. As a result, there is a discontinuity in the variation of a_c/Z with μ at the flow-arrest transition, as also seen in the inset of Fig. 4b. Such a rapid increase of contact anisotropy in high shear rate granular flows was also demonstrated previously [39]. Therefore, while ϕ or Z can completely characterize the state of shear flow in granular materials, a_c/Z is a key constitutive variable that uniquely characterizes both shear-arrested and shear flowing states of granular materials, and is remarkably insensitive to the applied pressure (see *SI Appendix*). These results provide crucial inputs towards the development of a unified constitutive model of granular materials that is applicable across its solid and fluid states of existence.

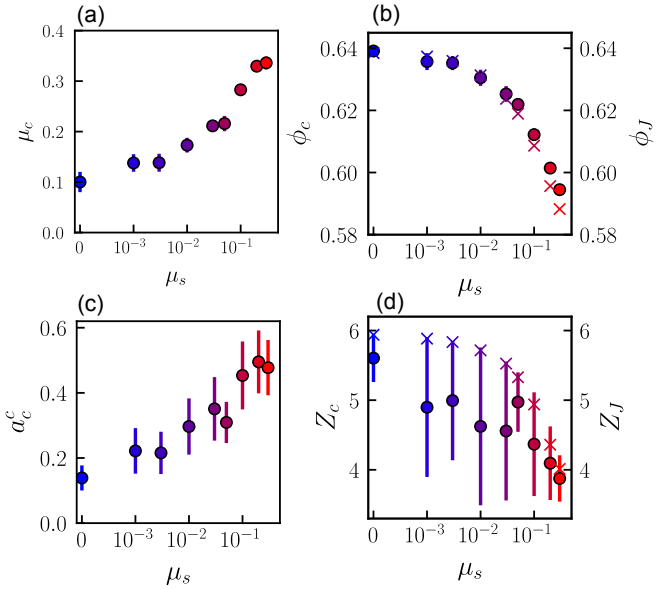

FIG. 5. Critical values (a) μ_c, (b) ϕ_c, (c) a_c^c and (d) Z_c as a function of friction μ_s. The jamming volume fraction ϕ_J and coordination number Z_J are also marked with crosses in (b) and (d) respectively. The leftmost data points in (a) - (d) correspond to the frictionless case. The vertical bars around data points represent the error in estimating the critical boundary between the steady shear flowing and shear arrested granular states from the discrete simulation data in Figs. 2a and 4.

Critical States at the Flow-Arrest Transition

Simulations under controlled pressure and shear stress facilitate a seamless transition between shear-arrested and shear-flowing states of granular materials. Such simulations are well-suited for identifying the critical boundary that separates these two nonequilibrium states. From the state diagrams described above, we extract friction-dependent critical values of volume fraction ϕ_c, stress ratio μ_c, coordination Z_c and contact anisotropy a_c^c at the flow-arrest transition. The critical stress ratio μ_c varies monotonically with μ_s, and ranges from 0.1 ± 0.02 for frictionless particles to 0.34 ± 0.01 for particles with high friction, as shown in Fig. 5a. The variation of μ_c with μ_s also corresponds well with previous simulations that more precisely characterized the critical transition from the power-law divergence of the time to arrest [26]. The critical μ_c corresponds to the dynamical arrest of granular flows, i.e., the minimum shear stress required to continue flowing a granular material indefinitely. Although this critical shear stress ratio is considered equal to the value required to start a granular flow in standard granular rheological models [1], recent experiments [44] and simulations [36] have identified a mild hysteresis in granular rheology that can result in different μ_c depending on whether the flow-arrest boundary is reached from a flowing state or an arrested state (such as in start-up shear tests).

The critical volume fraction ϕ_c at the flow-arrest transition decreases monotonically with friction, and ranges from $\phi_c = 0.64$ for frictionless particles to $\phi_c = 0.59$ for particles with high friction, as shown in Fig. 5b. Frictionless particles can flow at their densest random closed pack volume fraction, whereas the presence of friction necessarily requires dilation for steady flow. If the dilation of the granular material containing frictional particles is restricted and the material is forced to flow in a volume- and strain-controlled setup, as described in previous simulations [18, 45] and experiments [6], the flow will be chaotic and prone to instabilities. Such frustrated dilatancy effects have also been proposed to cause discontinuous shear thickening in dense suspensions [6]. As shown in Fig. 5b, ϕ_c is nearly equal to the isotropic jamming volume fraction ϕ_J, thus demonstrating that shear arrest of granular materials occurs at a well-defined volume fraction.

Unlike the volume fraction, a precise determination of the critical Z_c at the flow-arrest boundary is challenging because the granular material loses a significant number of contacts upon the beginning of flow. This is demonstrated in Fig. 5d, where the critical coordination Z_c is consistently lower than the isotropic jamming coordination Z_J, and they both decrease with friction. For frictionless particles $Z_J = 5.94$ and $Z_c = 5.6 \pm 0.34$ whereas $Z_J = 4.01$ and $Z_c = 3.88 \pm 0.33$ for particles with high friction. The large error bars associated with Z_c indicate that the loss of coordination during transition from arrested states to flowing states has significant variability across simulations, resulting from random breaking and forming of contacts during steady shear flow.

The critical contact fabric anisotropy a_c^c denotes the maximum anisotropy—i.e., maximum structural alignment on the contact network in the shear direction—that a granular material can sustain above which it will necessarily flow. The critical anisotropy increases with friction and ranges from $a_c^c = 0.14 \pm 0.03$ for friction-

less particles to $a_c^c = 0.48 \pm 0.08$ for particles with high friction, as shown in Fig. 5c. The increase of a_c^c with μ_s is expected as the tangential force of friction between particles provides increased stability to a highly sheared but static granular network. Furthermore, the mechanical stability of such highly sheared systems has also been recently demonstrated in experiments on shear jamming where the application of shear strain introduces directional rigidity in frictional granular systems at volume fractions below the isotropic frictionless jamming volume fraction [10]. Shear jamming can not be observed in the present simulations because the material is allowed to dilate or contract under constant pressure conditions, and a sheared granular material at low volume fractions will necessarily compact towards a shear arrested state or dilate towards steady shear flow depending on the applied stress and pressure. However, it is expected that the phenomenon of shear arrest at constant pressure simulated in this work is intimately related to the phenomenon of shear jamming at constant volume, which was also hypothesized in shear jamming experiments [10].

The non-zero value of a_c^c for frictionless particles, as shown in Fig. 5c, highlights that even dense frictionless granular systems can sustain a limited amount of structural anisotropy without yielding to flow. In the absence of friction and in the limit of hard particle stiffness, the origins of such non-zero yield stress are purely geometrical in nature [46]. Furthermore, these results indicate that the phenomenon of shear jamming can be observed for frictionless particles as well. Recent computational investigations have confirmed shear jamming like behavior in frictionless systems [47] along with connections to shear dilatancy [48] that is ubiquitous in frictional systems but can also occur in frictionless systems [49].

SUMMARY AND OUTLOOK

In summary, we have characterized nonequilibrium arrested and flowing states of stressed granular materials using a recently developed novel stress-controlled simulation method. We have constructed a flow-arrest state diagram for bulk granular materials under conditions of constant external shear stress and pressure, and identified the critical boundary demarcating the flow-arrest transition. We have demonstrated that while there exists a unique one-to-one relationship between internal stress ratio, volume fraction and coordination number for flowing states, an additional high-order structural descriptor in the form of contact fabric tensor is required to characterize shear-arrested states. This finding has important implications towards the development of constitutive models of granular materials that are applicable across their solid-like and fluid-like state of existence. We expect that contact fabric anisotropy is an important state variable that needs to be included in such constitutive modeling, and recent investigations on transient granular flows confirm these expectations [50, 51]. An important part of our future work involves the investigation of transient evolution of granular states prior to flow-arrest transition (such as shown in Fig. 1b) through cyclic stress-controlled shearing simulations that will extend the current analysis to unsteady granular flow phenomena.

Our work describes the conditions under which flowing granular materials can arrest along with the structural and mechanical properties of shear-arrested granular states. An important implication of the flow-arrest transition is observed in discontinuous shear thickening of dense suspensions, where the dynamical arrest of a flowing suspension is caused by frustrated dilatancy [6] and frictional transition within the contact network [22]. Because this phenomenon is sensitive to boundary and external stress conditions [6, 23, 24, 27], our simulation method is particularly well-suited to disentangle the role of boundaries from the bulk rheological instability in such dense suspensions. Extending the simulation studies of sheared dense suspensions [52, 53] to a fully-periodic and stress-controlled framework described here will be illuminating in this regard, and it constitutes an important part of our future work.

We have focused exclusively on granular materials in which sliding friction is the sole frictional phenomena. However, recent simulations have indicated that additional frictional modes such as rolling friction that are ubiquitous in granular materials have a dominant impact on their shear thickening [54] and jamming behavior [41]. Investigating the impact of such additional frictional modes on the flow-arrest transition is an important future work that will provide better predictions in practical applications of granular materials.

ACKNOWLEDGMENTS

I. Srivastava acknowledges support from the U.S. Department of Energy, Office of Science, Office of Advanced Scientific Computing Research, Applied Mathematics Program under contract No. DE-AC02-05CH11231. This work was performed at the Center for Integrated Nanotechnologies, a U.S. Department of Energy and Office of Basic Energy Sciences user facility. Sandia National Laboratories is a multimission laboratory managed and operated by National Technology and Engineering Solutions of Sandia, LLC, a wholly owned subsidiary of Honeywell International, Inc., for the U.S. Department of Energy's National Nuclear Security Administration under Contract No. DE-NA-0003525. This paper describes objective technical results and analysis. Any subjective views or opinions that might be expressed in the paper do not necessarily represent the views of the U.S. Department of Energy or the United States Government.

Appendix A: Materials and Methods

Stress-controlled simulation method

We use a stress-controlled simulation method where the triclinic periodic simulation cell denoted by a matrix $\boldsymbol{H}(t)$ and the positions and momenta of N particles $\{\boldsymbol{r}_k(t), \boldsymbol{p}_k(t)\}$ for $0 < k < N$ are evolved in time t as a response to the action of external applied stress tensor $\boldsymbol{\sigma}_a$ that is constrained by (i) $(1/3)\,\sigma_{a,ii} = p_a$, (ii) $\sigma_{a,ij} = \tau_a$ for $i, j = 1, 2$ and $2, 1$, and (iii) $\sigma_{a,ij} = 0$ for all other Einstein indices $i \neq j$. The triclinic periodic cell $\boldsymbol{H}$ is a concatenation of the three unit cell vectors that define the periodicity of the system. Under the action of applied traction at the boundaries of the periodic cell, it can dilate (or compact) and deform its shape in all possible ways, thus simulating the true bulk response of the granular material under external shear stress τ_a and pressure p_a. The reader is referred to ref. [16] for a detailed description of the simulation method including the equations of motion and the numerical method for their solution. All the simulations are performed using the large-scale molecular dynamics software LAMMPS [55].

The motion of the triclinic periodic cell $\boldsymbol{H}(t)$ results in a bulk velocity gradient $\nabla \boldsymbol{v}(t) = \dot{\boldsymbol{H}}(t)\boldsymbol{H}^{-1}(t)$ from which a symmetric strain rate tensor is computed as $\boldsymbol{D}(t) = \nabla \boldsymbol{v}(t) + \nabla \boldsymbol{v}^T(t)$. In steady state, $\boldsymbol{D}(t)$ is traceless, and a deviatoric strain rate is computed as $\dot{\gamma}(t) = \sqrt{\frac{1}{2}\boldsymbol{D}(t) : \boldsymbol{D}(t)}$ [16].

The internal Cauchy stress of the system $\boldsymbol{\sigma}$ is computed from the interparticle forces between two contacting particles with center-to-center contact vector $\boldsymbol{r}_c$ and total contact force $\boldsymbol{f}_c$ as:

$$\boldsymbol{\sigma} = \sum_{N_c} \boldsymbol{f}_c \otimes \boldsymbol{r}_c, \tag{A1}$$

where the sum is over all the contacts. The kinetic contributions to the internal stress are minimal in these dense flows and ignored. The internal pressure is computed as $p = \frac{1}{3}\sum_i \sigma_{ii}$, and the total internal shear stress is computed as $\tau = \sqrt{\frac{1}{2}\boldsymbol{\tau} : \boldsymbol{\tau}}$, where $\boldsymbol{\tau} = \boldsymbol{\sigma} - p\boldsymbol{I}$, and $\boldsymbol{I}$ is the identity matrix. During steady flow the Cauchy stress $\boldsymbol{\sigma}$ is not necessarily equal to $\boldsymbol{\sigma}_a$ (which is the Piola-Kirchoff measure of the stress) and the two are related by the bulk deformation gradient tensor $\boldsymbol{F}$ as: $\boldsymbol{\sigma} = (1/J)\,\boldsymbol{F}\boldsymbol{\sigma}_a\boldsymbol{F}$, where the Jacobian $J = \det[\boldsymbol{F}]$ [16].

Contact fabric tensor

A second-rank contact fabric tensor $\boldsymbol{A}_c$ is defined such that it provides a convenient description of the directional distribution of the particle contact network. It can be expressed as the coefficient of the second-order Fourier expansion of the orientational distribution function $P(\boldsymbol{n})$ of unit vectors $\boldsymbol{n}$ connecting two contacting particles:

$$P(\boldsymbol{n}) = \frac{1}{4\pi}\left[1 + \boldsymbol{A}_c : (\boldsymbol{n} \otimes \boldsymbol{n})\right]. \tag{A2}$$

Here, $\boldsymbol{A}_c$ is traceless and symmetric, and a scalar anisotropy measure is defined as $a_c^c = \sqrt{\frac{1}{2}\boldsymbol{A}_c : \boldsymbol{A}_c}$. The reader is referred to refs. [16, 30] for more details.

Appendix B: Flow-arrest state diagrams at different pressures

The flow-arrest state diagrams in the main text correspond to an external applied pressure of $p_a = 10^{-5}$. In this Supporting Information we provide similar diagrams for a higher and a lower applied pressure: $p_a = 10^{-4}$ and $p_a = 10^{-6}$. Additionally, we also extract the critical values at the flow-arrest transition boundary at these applied pressures, which are shown in Fig. 8. In Figs. 6 and 7, we show the flow-arrest state diagrams along various axes described in Figs. 2 and 3 of the main text. Evidently the states of flow and arrest and the boundary defining the flow-arrest transition remains similar at all pressures, thus confirming our assumption that the present results correspond to a hard-particle limit. At lower pressures (corresponding to stiffer particles), the stress-controlled simulation method requires substantially longer simulation runs to achieve steady state and to extract reasonable statistics concerning the material microstructure. This is seen by the large error bars associated with identifying a_c^c and Z_c for the the case of $p_a = 10^{-6}$ in Fig. 8. Furthermore, we note that although the critical stress ratio μ_c and critical volume fraction ϕ_c remain insensitive to the applied pressure, the coordination numbers, both at jamming Z_c and at the flow-arrest transition Z_c, are more sensitive to the applied pressure, as seen in Figs. 8(d) and (h). At lower pressures the coordination number is consistently lower for both flowing and arrested states, which can be observed by comparing Fig. 6(c) and Fig. 7(c). Remarkably, however, the variation of ratio a_c/Z with μ is nearly equivalent at all pressures (see Fig. 6(d) and Fig. 7(d)), thus further confirming that a_c/Z is an important internal constitutive variable in modeling the flow-arrest transition of granular materials.

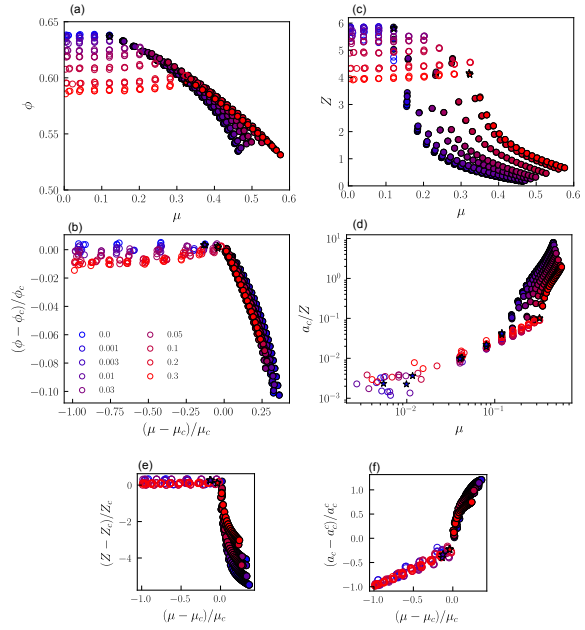

FIG. 6. (a) Nonequilibrium states of shear arrest (open symbols) and steady shear flow (closed symbols) on (a) $\phi-\mu$ axes and (c) $Z-\mu$ axes for different frictions μ_s (see the color legend in (b)) for an applied pressure $p_a = 10^{-6}$. The asterisk denote states in the vicinity of the flow-arrest transition for which some simulations arrested and some flowed steadily at long times. (b) The state diagram in (a) shifted and normalized by the friction-dependent critical values μ_c and ϕ_c. (d) Contact fabric anisotropy a_c normalized by Z for the states of steady flow and arrest as a function of μ. (e) The state diagram in (c) shifted and normalized by the friction-dependent critical values Z_c and μ_c. (f) The state diagram in (d) shifted and normalized by the friction-dependent critical values a_c^c and μ_c.

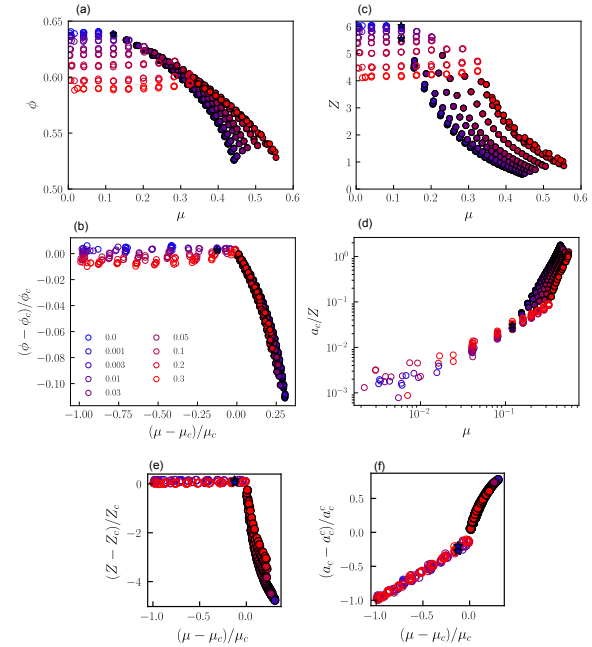

FIG. 7. (a) Nonequilibrium states of shear arrest (open symbols) and steady shear flow (closed symbols) on (a) $\phi-\mu$ axes and (c) $Z-\mu$ axes for different frictions μ_s (see the color legend in (b)) for an applied pressure $p_a = 10^{-4}$. The asterisk denote states in the vicinity of the flow-arrest transition for which some simulations arrested and some flowed steadily at long times. (b) The state diagram in (a) shifted and normalized by the friction-dependent critical values μ_c and ϕ_c. (d) Contact fabric anisotropy a_c normalized by Z for the states of steady flow and arrest as a function of μ. (e) The state diagram in (c) shifted and normalized by the friction-dependent critical values Z_c and μ_c. (f) The state diagram in (d) shifted and normalized by the friction-dependent critical values a_c^c and μ_c.

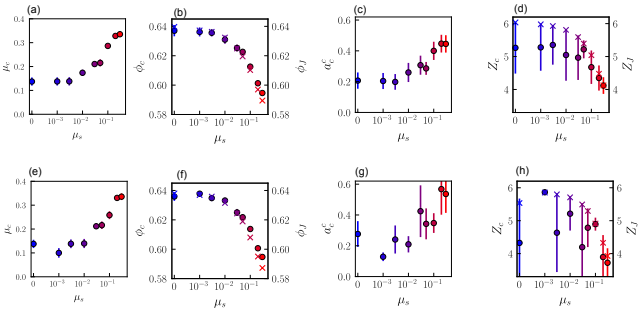

FIG. 8. Critical values (a,e) μ_c, (b,f) ϕ_c, (c,g) a_c^c and (d,h) Z_c as a function of friction μ_s. The top row corresponds to applied pressure $p_a = 10^{-4}$ and the bottom row corresponds to $p_a = 10^{-6}$. The jamming volume fraction ϕ_J and coordination number Z_J are also marked with crosses in (b,f) and (d,h) respectively. The leftmost data points in each panel correspond to the frictionless case. The vertical bars around data points represent the error in estimating the critical boundary between the steady shear flowing and shear arrested granular states from the discrete simulation data in Figs. 6 and 7.

[1] Y. Forterre and O. Pouliquen, Flows of dense granular media, Annual Review of Fluid Mechanics **40**, 1–24 (2008).

[2] C. H. Scholz, Earthquakes and friction laws, Nature **391**, 37–42 (1998).

[3] A. Lucas, A. Mangeney, and J. P. Ampuero, Frictional velocity-weakening in landslides on earth and on other planetary bodies, Nature Communications **5**, 3417 (2014).

[4] I. Zuriguel, D. R. Parisi, R. C. Hidalgo, C. Lozano, A. Janda, P. A. Gago, J. P. Peralta, L. M. Ferrer, L. A. Pugnaloni, E. Clément, D. Maza, I. Pagonabarraga, and A. Garcimartín, Clogging transition of many-particle systems flowing through bottlenecks, Scientific Reports **4**, 7324 (2014).

[5] A. H. Clark, M. D. Shattuck, N. T. Ouellette, and C. S. O'Hern, Onset and cessation of motion in hydrodynamically sheared granular beds, Physical Review E **92**, 042202 (2015).

[6] E. Brown and H. M. Jaeger, The role of dilation and confining stresses in shear thickening of dense suspensions, Journal of Rheology **56**, 875–923 (2012).

[7] I. R. Peters, S. Majumdar, and H. M. Jaeger, Direct observation of dynamic shear jamming in dense suspensions, Nature **532**, 214–217 (2016).

[8] H. M. Jaeger, S. R. Nagel, and R. P. Behringer, Granular solids, liquids, and gases, Reviews of Modern Physics **68**, 1259 (1996).

[9] A. J. Liu and S. R. Nagel, Jamming is not just cool any more, Nature **396**, 21–22 (1998).

[10] D. Bi, J. Zhang, B. Chakraborty, and R. P. Behringer, Jamming by shear., Nature **480**, 355–358 (2011).

[11] A. J. Kabla and T. J. Senden, Dilatancy in slow granular flows., Physical Review Letters **102**, 228301 (2009).

[12] F. Boyer, E. Guazzelli, and O. Pouliquen, Unifying suspension and granular rheology, Physical Review Letters **107**, 188301 (2011).

[13] C. Clavaud, A. Bérut, B. Metzger, and Y. Forterre, Revealing the frictional transition in shear-thickening suspensions, Proceedings of the National Academy of Sciences **114**, 5147–5152 (2017).

[14] F. Da Cruz, S. Emam, M. Prochnow, J. N. Roux, and F. Chevoir, Rheophysics of dense granular materials: Discrete simulation of plane shear flows., Physical Review E **72**, 021309 (2005).

[15] P. E. Peyneau and J. N. Roux, Frictionless bead packs have macroscopic friction, but no dilatancy., Physical Review E **78**, 011307 (2008).

[16] I. Srivastava, L. E. Silbert, G. S. Grest, and J. B. Lechman, Viscometric flow of dense granular materials under controlled pressure and shear stress, Journal of Fluid Mechanics **907**, A18 (2021).

[17] A. Schofield and P. Wroth, *Critical state soil mechanics*, Vol. 310 (McGraw-Hill, 1968).

[18] M. Otsuki and H. Hayakawa, Critical scaling near jamming transition for frictional granular particles., Physical Review E **83**, 051301 (2011).

[19] M. P. Ciamarra, R. Pastore, M. Nicodemi, and A. Coniglio, Jamming phase diagram for frictional particles., Physical Review E **84**, 041308 (2011).

[20] M. Grob, A. Zippelius, and C. Heussinger, Rheological chaos of frictional grains., Physical Review E **93**, 030901 (2016).

[21] A. Fall, N. Huang, F. Bertrand, G. Ovarlez, and D. Bonn, Shear thickening of cornstarch suspensions as a reentrant jamming transition., Physical Review Letters **100**, 018301 (2008).

[22] M. Wyart and M. E. Cates, Discontinuous shear thickening without inertia in dense non-brownian suspensions., Physical Review Letters **112**, 098302 (2014).

[23] J. Dong and M. Trulsson, Analog of discontinuous shear thickening flows under confining pressure, Physical Review Fluids **2**, 081301 (2017).

[24] V. Rathee, D. L. Blair, and J. S. Urbach, Localized transient jamming in discontinuous shear thickening, Journal of Rheology **64**, 299–308 (2020).

[25] T. Kawasaki, D. Coslovich, A. Ikeda, and L. Berthier, Diverging viscosity and soft granular rheology in non-brownian suspensions, Physical Review E **91**, 012203 (2015).

[26] I. Srivastava, L. E. Silbert, G. S. Grest, and J. B. Lechman, Flow-arrest transitions in frictional granular matter, Physical Review Letters **122**, 048003 (2019).

[27] M. Wang and J. F. Brady, Constant stress and pressure rheology of colloidal suspensions., Physical Review Letters **115**, 158301 (2015).

[28] P. Schall and M. Van Hecke, Shear bands in matter with granularity, Annual Review of Fluid Mechanics **42**, 67–88 (2010).

[29] D. L. Henann and K. Kamrin, A predictive, size-dependent continuum model for dense granular flows., Proceedings of the National Academy of Sciences **110**, 6730–6735 (2013).

[30] I. Srivastava, J. B. Lechman, G. S. Grest, and L. E. Silbert, Evolution of internal granular structure at the flow-arrest transition, Granular Matter **22**, 41 (2020).

[31] L. E. Silbert, Jamming of frictional spheres and random loose packing, Soft Matter **6**, 2918 (2010).

[32] A. Favier De Coulomb, M. Bouzid, P. Claudin, E. Clément, and B. Andreotti, Rheology of granular flows across the transition from soft to rigid particles, Physical Review Fluids **2**, 102301 (2017).

[33] S. Kim and K. Kamrin, Power-law scaling in granular rheology across flow geometries, Physical Review Letters **125**, 088002 (2020).

[34] C. K. K. Lun, S. B. Savage, D. J. Jeffrey, and N. Chepurniy, Kinetic theories for granular flow: Inelastic particles in couette flow and slightly inelastic particles in a general flowfield, Journal of Fluid Mechanics **140**, 223–256 (1984).

[35] L. Bocquet, W. Losert, D. Schalk, T. C. Lubensky, and J. P. Gollub, Granular shear flow dynamics and forces: Experiment and continuum theory, Physical Review E **65**, 011307 (2001).

[36] E. Degiuli and M. Wyart, Friction law and hysteresis in granular materials., Proceedings of the National Academy of Sciences **114**, 9284–9289 (2017).

[37] K. M. Salerno, D. S. Bolintineanu, G. S. Grest, J. B. Lechman, S. J. Plimpton, I. Srivastava, and L. E. Silbert, Effect of shape and friction on the packing and flow of granular materials, Physical Review E **98**, 050901 (2018).

[38] C. P. Goodrich, A. J. Liu, and J. P. Sethna, Scaling ansatz for the jamming transition., Proceedings of the National Academy of Sciences **113**, 9745–9750 (2016).

[39] E. Azéma and F. Radjaï, Internal structure of inertial granular flows., Physical Review Letters **112**, 078001 (2014).

[40] J. Sun and S. Sundaresan, A constitutive model with microstructure evolution for flow of rate-independent granular materials, Journal of Fluid Mechanics **682**, 590–616 (2011).

[41] A. P. Santos, D. S. Bolintineanu, G. S. Grest, J. B. Lechman, S. J. Plimpton, I. Srivastava, and L. E. Silbert, Granular packings with sliding, rolling, and twisting friction, Physical Review E **102**, 032903 (2020).

[42] F. Radjai, J.-Y. Delenne, E. Azéma, and S. Roux, Fabric evolution and accessible geometrical states in granular materials, Granular Matter **14**, 259–264 (2012).

[43] F. Radjai, D. E. Wolf, M. Jean, and J.-J. Moreau, Bimodal character of stress transmission in granular packings, Physical Review Letters **80**, 61 (1998).

[44] H. Perrin, C. Clavaud, M. Wyart, B. Metzger, and Y. Forterre, Interparticle friction leads to nonmonotonic flow curves and hysteresis in viscous suspensions, Physical Review X **9**, 031027 (2019).

[45] C. Heussinger, Shear thickening in granular suspensions: Interparticle friction and dynamically correlated clusters, Physical Review E **88**, 050201 (2013).

[46] J.-N. Roux, Geometric origin of mechanical properties of granular materials, Physical Review E **61**, 6802 (2000).

[47] H. A. Vinutha and S. Sastry, Disentangling the role of structure and friction in shear jamming, Nature Physics **12**, 578–583 (2016).

[48] P. Das, H. A. Vinutha, and S. Sastry, Unified phase diagram of reversible–irreversible, jamming, and yielding transitions in cyclically sheared soft-sphere packings, Proceedings of the National Academy of Sciences **117**, 10203–10209 (2020).

[49] V. Babu, D. Pan, Y. Jin, B. Chakraborty, and S. Sastry, Dilatancy, shear jamming, and a generalized jamming phase diagram of frictionless sphere packings, Soft Matter **17**, 3121–3127 (2021).

[50] R. N. Chacko, R. Mari, S. M. Fielding, and M. E. Cates, Shear reversal in dense suspensions: The challenge to fabric evolution models from simulation data, Journal of Fluid Mechanics **847**, 700–734 (2018).

[51] E. R. Parra and K. Kamrin, Capturing transient granular rheology with extended fabric tensor relations, Granular Matter **21**, 89 (2019).

[52] R. Mari, R. Seto, J. F. Morris, and M. M. Denn, Discontinuous shear thickening in brownian suspensions by dynamic simulation, Proceedings of the National Academy of Sciences **112**, 15326–15330 (2015).

[53] A. Singh, R. Mari, M. M. Denn, and J. F. Morris, A constitutive model for simple shear of dense frictional suspensions, Journal of Rheology **62**, 457–468 (2018).

[54] A. Singh, C. Ness, R. Seto, J. J. De Pablo, and H. M. Jaeger, Shear thickening and jamming of dense suspensions: The "roll" of friction, Physical Review Letters **124**, 248005 (2020).

[55] S. Plimpton, Fast parallel algorithms for short-range molecular dynamics, Journal of Computational Physics **117**, 1 (1995).